Humidity-Responsive Actuator with Viewable and Programmable Deformation Enabled by Tannic Acid as Physical Cross-linker

Junbo Guo, Hao Zhang, Tiantian Cui, Jiawei Li, Min-Hui Li, Jun Hu

Humidity-Responsive Actuator with Viewable and Programmable Deformation Enabled by Tannic Acid as Physical Crosslinker

*Junbo Guo, Hao Zhang, Tiantian Cui, Jiawei Li, Min-Hui Li, and Jun Hu**

J. Guo, H. Zhang, T. Cui, J. Li, J. Hu
Beijing Advanced Innovation Center for Soft Matter Science and Engineering, Beijing University of Chemical Technology, North Third Ring Road 15, Chaoyang District, Beijing 100029, China
E-mail: jhu@mail.buct.edu.cn

M.-H. Li
Chimie ParisTech, PSL University, CNRS, Institut de Recherche de Chimie Paris, 11 rue Pierre et Marie Curie, Paris 75005, France

Keywords: humidity-driven actuator, controllable deformation, in-situ visualization, patterned monolayer film, tannic acid

Programmable humidity-driven actuators can autonomously transform into predefined forms in reaction to environmental stimuli, which are appealing for the creation of intelligent devices. Here, we report a viewable in-situ programmed humidity-driven monolayer actuator consisting of hydrophilic poly(vinyl alcohol) (PVA), polyacrylamide (PAAm), and tannic acid (TA). Benefiting from the multiple hydrogen bonding of TA with PVA and PAAm, TA acts as a physical crosslinker to precisely control the modulus distribution of the monolayer film when introducing patterns by TA in the polymer film. Moreover, the physical anchoring effect of TA to PVA and PAAm makes TA molecules highly fluorescent in solid state. The resulting PVA/PAAm/TA film simultaneously exhibits high optical transparency (>80%), good mechanical property (tensile stress at break of 75.0 MPa, Young′s modulus of 7.1 GPa), bright cyan fluorescence, and reversible fast humidity-response (0.04 s) under the relative humidity difference (ΔRH) of 55%. After in-plane patterning, the film actuator can bend towards controllable directions in response to humidity gradient, and its programmed mode can be viewed by the fluorescence under UV light. This viewable and programmable approach will substantially aid the design of humidity-driven actuators for applications in the fields of biomimicry, artificial muscles, and intelligent switches.

1. Introduction

Natural species including both animals and plants have the instinct to adapt to their environment for their survive. For instance, Venus flytrap and Mimosa pudica shut leaves after insects reach their traps,[1-3] whereas pine cones and petunias open and close in response to variations in humidity.[4,5] These wondrous events inspire researchers to mimic material properties when designing intelligent actuators.[6-10] Among them, humidity-driven actuators have drawn ongoing interest in recent years because they can transform chemical energy into mechanical energy triggered by water evaporation or humidity change that occurs frequently in nature.[11-14] As the raw materials for humidity-driven actuators only need to have hydrophilic groups like hydroxyl, amino, carboxyl, etc. in their structures, it is easy to build these actuators on a large scale. Therefore, humidity-driven actuators are appealing for the use in smart windows,[15] artificial muscles,[16] soft robotics,[17] and energy-harvesting devices.[18,19]

There are typically two strategies to design humidity-driven actuators mimicking the internal heterogeneous architectures of creatures that give them the ability to achieve specific shape morphing in response to humidity.[20,21] In the first strategy, bilayer or multilayer structures consisted of hydrophilic and hydrophobic hybrid materials are usually fabricated to achieve the difference in hydrophilicity across materials for the realization of deformation and energy conversion.[22-24] However, these bilayer or multilayer actuators often suffer from strength mismatch and delamination among layers, which in turn lead to poor interlayer adhesion during the frequent bending processes. Besides, they are often incapable of performing complex motions except for simple unidirectional bending. In the second strategy, the monolayer structure is only made of hydrophilic substances that react to inhomogeneous humidity stimulus.[25-27] Benefiting from the intrinsic swelling/shrinking difference within hydrophilic substances triggered by anisotropic exposure to humidity, the monolayer actuators have the advantages of large deformation, high response efficiency, and good actuation stability. Moreover, they allow in-plane patterning that is regarded as one of the best options to create precise humidity-driven actuators because of the possibility to design preprogrammed actuations. For instance, Huang et al. reported a humidity-driven film containing photosensitive coumarin pendant groups. Promoted by the patterned photodimerization of coumarin groups, the humidity-responsive deformation was well regulated by the modulus distribution inside the film.[28] Zhao et al. developed a polyethylene-co-acrylic acid polymer film with programmable humidity-driven actuations, as the distribution of hydrophilic and hydrophobic areas inside the film was precisely created by the local surface treatment using acid or alkali.[29] Notably, despite these impressive advancements, the majority of monolayer actuators are often made of synthetic

polymers, which are costly and time-consuming. Moreover, it is difficult to match the programming mode with the actuation mode under an in-situ viewable method, which is important for interactive biofeedback, particularly in transparent actuators.[30-32] Thus, it is necessary to develop monolayer actuators that can respond quickly to humidity changes and meanwhile allow for in-situ programming visualization.

In this work, we report a viewable and programmable humidity-driven film actuator consisting of all commercially available and hydrophilic substances, *i.e.*, poly(vinyl alcohol) (PVA), polyacrylamide (PAAm), and tannic acid (TA). As a natural polyphenol, TA has abundant phenol groups that can easily link with hydrophilic polymers through multiple hydrogen bonds, enhancing mechanical performance and affording a controlled modulus distribution when patterning polymer films.[33] More importantly, the anchoring of TA to polymers forming physical crosslinking knots makes TA molecules brightly fluorescent in solid state.[34] The resulting PVA/PAAm/TA film simultaneously exhibits high optical transparency (>80%), good mechanical property (tensile stress at break of 75.0 MPa, Young′s modulus of 7.1 GPa), cyan fluorescence, and fast reversible humidity-response (0.04 s). After in-plane patterning with a controlled mode, the patterned-PVA/PAAm/TA film can bend in different manners in response to humidity gradient, and the programmed mode can be directly illuminated under UV light. Therefore, this humidity-driven actuator has promising potential applications in walking devices and smart mechanical lifts.

2. Results and Discussion

2.1 Fabrication and characterization of the PVA/PAAm film

Figure 1a depicted our consecutive fabrication process of the PVA/PAAm film for humidity-driven actuation. Initially, PVA, AAm, N,N′-methylenebis(acrylamide) (MBA), and ammonium persulphate (APS) were dissolved in deionized water (DI water). Later, the solution was packed into a glass mold and thermally polymerized in an oven at 60°C for 90 min, affording the transparent PVA/PAAm hydrogel with a semi-interpenetrating polymer network (SIPN). After biaxial pre-stretching the PVA/PAAm hydrogel followed by fixed drying, a series of monolayer films, named as PVA/PAAm$_x$, where x represented the stretch ratio of biaxial pre-stretching (2, 2.5, and 3), were successfully prepared with controllable thickness (Figure S1, Supporting Information).

The as-prepared PVA/PAAm film was colorless and transparent (Figure 1b), with an average transmittance of over 80% throughout the visible region from 400 to 800 nm. Scanning electron microscope (SEM) image showed that the surface microstructure of the film was flat and devoid

of pores and fissures (Figure 1c), revealing a homogeneous structure without phase separation. It can be further confirmed by atomic force microscope (AFM) image, where the root mean square roughness (R_a) was only 2.60 nm (Figure 1d). All these results were consistent with the high optical transparency of the PVA/PAAm film. Moreover, X-ray diffraction (XRD) was performed to distinguish the crystal structure of the PVA/PAAm film (Figure 1e). No crystalline peak of the PAAm film was observed, instead of a blunt peak at 2θ = 21.6°, because of its amorphous nature. On the contrary, there was a crystalline reflection at 19.6° in the neat PVA film, corresponding to the (101) plane of the semicrystalline structure.[35] The introduction of PAAm caused a reduction in the crystallization peak of the PVA/PAAm film, indicating that the crystalline structure of PVA was destroyed by the interpenetrating PAAm network.[36,37] Additionally, density functional theory (DFT) calculation was performed by using Gaussian 09 program, and the geometries of PVA and PAAm molecules were optimized at the B3LYP-D3(BJ)/def2-SVP level. Using the electron density at bond critical point (equation S1), the hydrogen bond strength of PVA-PAAm was then estimated up to -10.60 Kcal/mol (Figure 1f). As expected in the characteristic region and the fingerprint region of attenuated total reflection Fourier transform infrared spectroscopy (ATR-FTIR, Figure 1g and S2), the characteristic peaks at 1085 cm^{-1} for C-O stretching vibration from PVA and 1645 cm^{-1} for C=O stretching vibration from PAAm are all displayed in the spectrum of PVA/PAAm film. Compared with the neat PAAm, the N-H stretching peak of PVA/PAAm film shifted to a lower wavenumber of 3328 and 3182 cm^{-1} from 3333 and 3186 cm^{-1}, respectively, indicating the formation of hydrogen bonds that reduced the vibration energy.[38,39] In brief, the good hydrophilicity of PVA and PAAm and the strong hydrogen bonding within SIPN facilitated the structural uniformity of the PVA/PAAm film, which was essential to high transmittance and humidity-driven actuation.

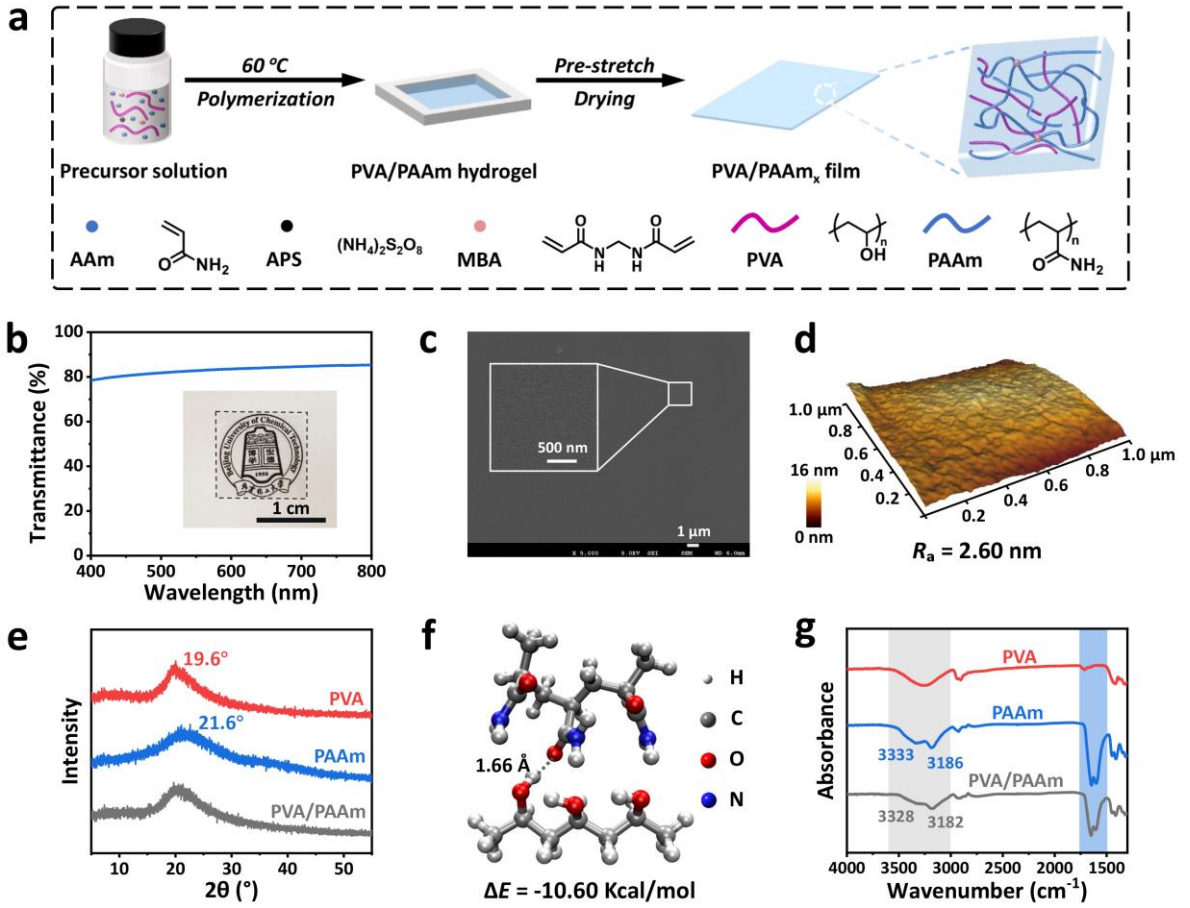

Figure 1. a) Schematic illustration of the fabrication of the PVA/PAAm$_x$ film. b) UV-vis spectrum of the PVA/PAAm$_{2.5}$ film. Inset shows the optical photo of the PVA/PAAm$_{2.5}$ film. c) Surface SEM image of the PVA/PAAm$_{2.5}$ film. Inset shows the local magnification. d) Surface AFM image of the PVA/PAAm$_{2.5}$ film. e) XRD patterns of PVA, PAAm, and PVA/PAAm$_{2.5}$ film. f) Hydrogen bonding interactions of PVA-PAAm obtained by DFT. The distance of the hydrogen bond is indicated by the dotted line. g) ATR-FTIR spectra of PVA, PAAm, and PVA/PAAm$_{2.5}$ film from 1300 to 4000 cm^{-1}.

2.2 Humidity-driven actuation performance of the PVA/PAAm film

In an asymmetric humidity gradient environment, the motivation of the PVA/PAAm film could be triggered. As shown in **Figure 2**a, the expose of the PVA/PAAm film to different relative humidity (RH) caused an asymmetric volume expansion, consequently leading to the curling of the film. During this humidity-driven motivation, the hydrophilic hydroxyl and amide groups and the hydrophobic polymer skeleton played a key role.[40] On one hand, the hydroxyl and amide groups on PVA and PAAm quickly absorbed water molecules, causing the PVA/PAAm film to swell. On the other hand, the polymer skeleton helped water molecules to desorb from the PVA/PAAm film. As a result, the PVA/PAAm film could swiftly absorb or desorb water,

with rapid swelling or shrinkage deformations, when the humidity in environment changed. This was further confirmed by control experiments in Movie S1, where the bending of polyethylene glycol/poly(N-isopropylacrylamide) (PEG/PNIPAm) film was slower than that of PVA/PAAm$_{2.5}$ film under the same condition, due to the reduction of hydroxyl and amide groups. Note that the absorption of water was the result of hydrogen bonding competition between polymer-water and polymer-polymer. Benefiting from this competition, the PVA/PAAm film owned the reversible humidity-driven ability, that is, hydrated under high humidity conditions while dehydrated under low humidity conditions. Figure 2b showed the bidirectional curling behavior for the PVA/PAAm film, where the humidity gradient provided by human finger made the PVA/PAAm film to continuously and reversibly bend, strongly revealing the dynamic hydrogen bonding between PVA/PAAm film and water molecules during the actuation process.

As the film thicknesses had a significant influence on the humidity-responsive performance, the humidity-driven behaviors of the PVA/PAAm$_2$, the PVA/PAAm$_{2.5}$, and the PVA/PAAm$_3$ films were quantitatively investigated under an identical relative humidity difference (ΔRH) of 55%. A schematic illustration of the reversible actuation behavior of the film was shown in the inset of Figure 2c, where θ denoted the bending angle of the film upon exposure to humidity gradient. Owing to the high sensitivity of hydrophilic groups, all the PVA/PAAm films can respond to humidity gradient within 0.04 s. The thin PVA/PAAm$_3$ film (~15 μm) had the fastest actuation response (Figure S3a, Supporting Information), where the bending angle rapidly increased within 3 s and reached the maximum of 65° at 7 s. After that, it began to fluctuate because the lower thickness caused PVA/PAAm$_3$ film to oscillate even under a slight fluctuation of humidity. Increasing film thickness would avoid this negative influence on bending angle (Figure S3b, Supporting Information), but the excessive thickness of PVA/PAAm$_2$ (~42 μm) film would reduce the maximum bending angle. Additionally, the bending angle of the PVA/PAAm$_2$ film was constantly increasing. As a result, it is impossible to attain a stable maximum bending angle for PVA/PAAm$_2$ film. This occurred as a result of the inability of water molecules to desorb from the thick film in time, progressively causing the cumulative bending. In contrast, the PVA/PAAm$_{2.5}$ film (~25 μm) with an optimal thickness both had the fast response speed and good stability to humidity gradient (Figure 2c). The whole bending process can be divided into three stages. In stage I, the PVA/PAAm$_{2.5}$ film displayed a quick response with an average bending speed of 11.12° s^{-1}. In stage II, the bending speed slowed down to 1.68°·s^{-1} and kept for 12 s. After that, the bending angle of the PVA/PAAm$_{2.5}$ film reached equilibrium of 87° in stage III. This phenomenon was caused by the diffusion

effect of water molecules. Initially, the concentration gradient caused water molecules to migrate towards the film when it was positioned in humidity gradient. This swelled the film and resulted in a high-speed bending at the beginning of actuation. As the diffusion advanced, the concentration difference of water molecules decreased, and the contact area between the film and water molecules reduced. As a result, the bending speed slowed down and could be maintained for a relatively long time. When the diffusion process reached equilibrium, the bending speed further declined until the actuation process ended. Upon the removal of humidity source, the PVA/PAAm$_{2.5}$ film could recover to its initial state (Figure 2d). The film dropped within 0.04 s after the humidity gradient was "off" at 20 s, and then progressively dropped to 78% of the maximum bending angle at 50 s. Obviously, the dynamic adsorption and desorption of water molecules was the key to this reversible bending. Once the humidity gradient was "off", a large number of the adsorbed water molecules on film surface desorbed because of the low humidity environment, resulting in a rapid drop in bending angle. After that, the water molecules inside the film began to desorb as well, yet in a slower desorption speed, consequently leading to a slow recovery rate of the PVA/PAAm$_{2.5}$ film.

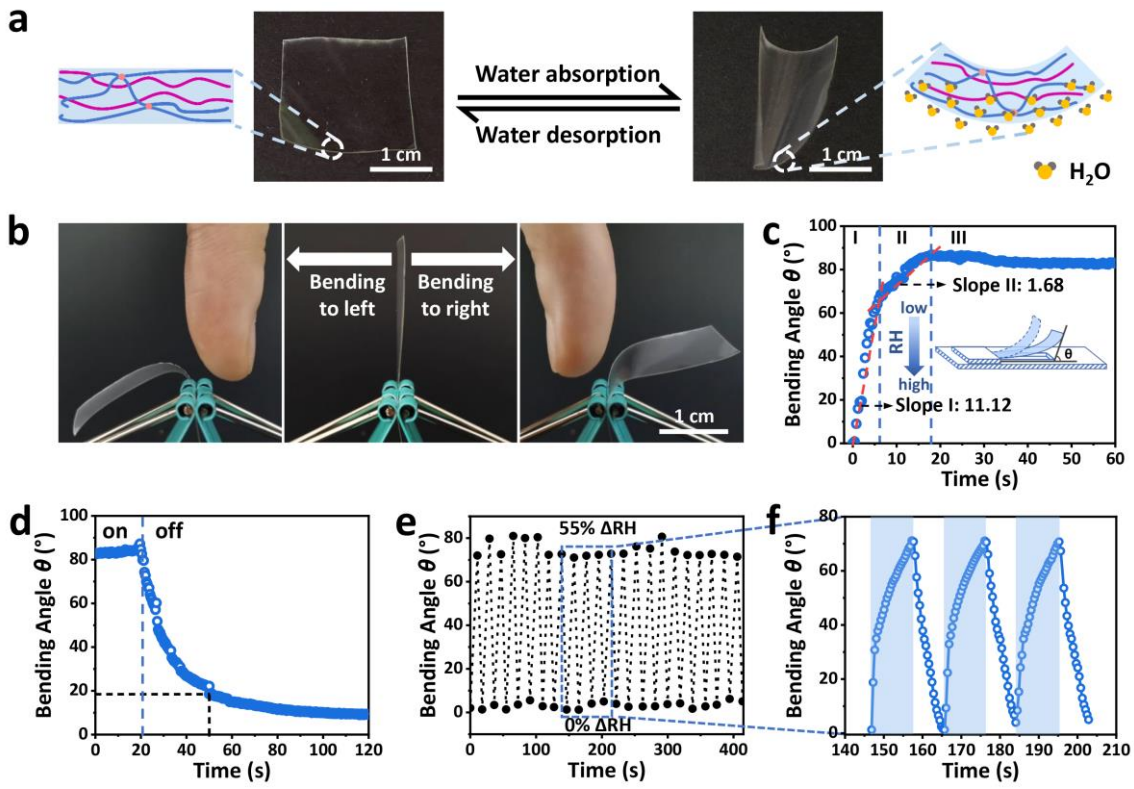

Figure 2. a) Scheme and photos of the PVA/PAAm$_{2.5}$ film before and after exposure to humidity. b) Photos showing a bidirectional motivation of the PVA/PAAm$_{2.5}$ film driven by the humidity gradient provided by human finger. c) Variation of bending angle (θ) of the PVA/PAAm$_{2.5}$ film upon exposure to ΔRH = 55%. Inset shows the schematic diagram of the

device for testing humidity responsivity with the decrease of RH from bottom to top. θ denotes the bending angle of the film upon exposure to humidity gradient, which is the angle between the tangent line of the curved film edge and the horizontal plane. d) Unbending motion of the PVA/PAAm$_{2.5}$ film after the removal of humidity gradient. e) The reversible motivation of the PVA/PAAm$_{2.5}$ film with continuous cycles of ΔRH = 55% and 0%. f) Three magnified cycles in e).

In addition, the motivation stability of the PVA/PAAm$_{2.5}$ film was evaluated (Figure 2e and 2f). Clearly, the reversible bending-unbending of the PVA/PAAm$_{2.5}$ film can be repeated over 20 times upon switching the ΔRH of 55% and 0%, without apparent fatigue in continuous actuation cycles. And after storing in the environment for 180 days, the PVA/PAAm$_{2.5}$ film still maintained the humidity-driven ability (Figure S4, Supporting Information). The PVA/PAAm$_2$ and PVA/PAAm$_3$ films could also achieve the comparable reversible cycles by varying exposure time to high and low humidity gradients (Figure S5, Supporting Information). Due to the inside layer of the thick film desorbed water molecules more slowly than the exterior layer, the PVA/PAAm$_2$ film took longer time (10 s) to return to the initial state than the thinner PVA/PAAm$_3$ film (5 s). As the PVA/PAAm$_{2.5}$ film simultaneously achieved stable and sensitive bending actuation in response to humidity gradient, it was used in the following research of the patterned film together with TA.

2.3 Fabrication and characterization of the fluorescent PVA/PAAm/TA film

To view the actuation mode, the fluorescent PVA/PAAm/TA film was produced by casting the TA aqueous solution (0.24 M) as ink on the PVA/PAAm film (**Figure 3**a). Thanks to the hydrogen bonding between TA and polymers, a homogeneous and well-bounded physical crosslinking network was established. The resulting PVA/PAAm/TA film showed an absorption from 230 to 360 nm due to the π-π* transition in the aromatic structure of TA, and owned an average transmittance of 83% throughout the visible region from 400 to 800 nm (Figure 3b). The high transparency of the PVA/PAAm/TA film was confirmed by SEM (Figure 3c) and AFM image (Figure 3d), where the R_a was 0.32 nm, only one-eighth that of the PVA/PAAm film. The considerable reduction in R_a was attributed to the creation of a dense crosslinking network and the destruction of the semicrystalline structure of PVA. As shown in Figure S6 (Supporting Information), the introduction of amorphous TA into PVA/PAAm film further reduced the crystallization peak of PVA because of the hydrogen bonds between PVA and TA.[41] ATR-FTIR spectra showed that the N-H stretching vibration of PVA/PAAm/TA downshifted to 3325 and 3180 cm^{-1} compared with those at 3328 and 3182 cm^{-1} of PVA/PAAm

(Figure S7, Supporting Information), strongly indicating the participation of phenolic hydroxyl groups of TA in hydrogen bonding interactions. More surprisingly, the PVA/PAAm/TA film had strong cyan emission under UV light (Figure 3e). The fluorescent images in Figure 3f and S8 (Supporting Information) demonstrated that the PVA, PAAm, and PVA/PAAm films had no fluorescence, while bright cyan fluorescence was observed for the PAAm/TA, PVA/TA, and PVA/PAAm/TA films. It is known that the physical anchoring of fluorescent molecules on polymers can effectively inhibit the aggregation of fluorescent molecules and avoid their self-quenching.[42-44] In our case, the physical crosslinking of polymer chains by TA was assumed to diminish the freedom degree of TA molecules, thus avoiding the aggregation and the self-quenching of TA molecules.

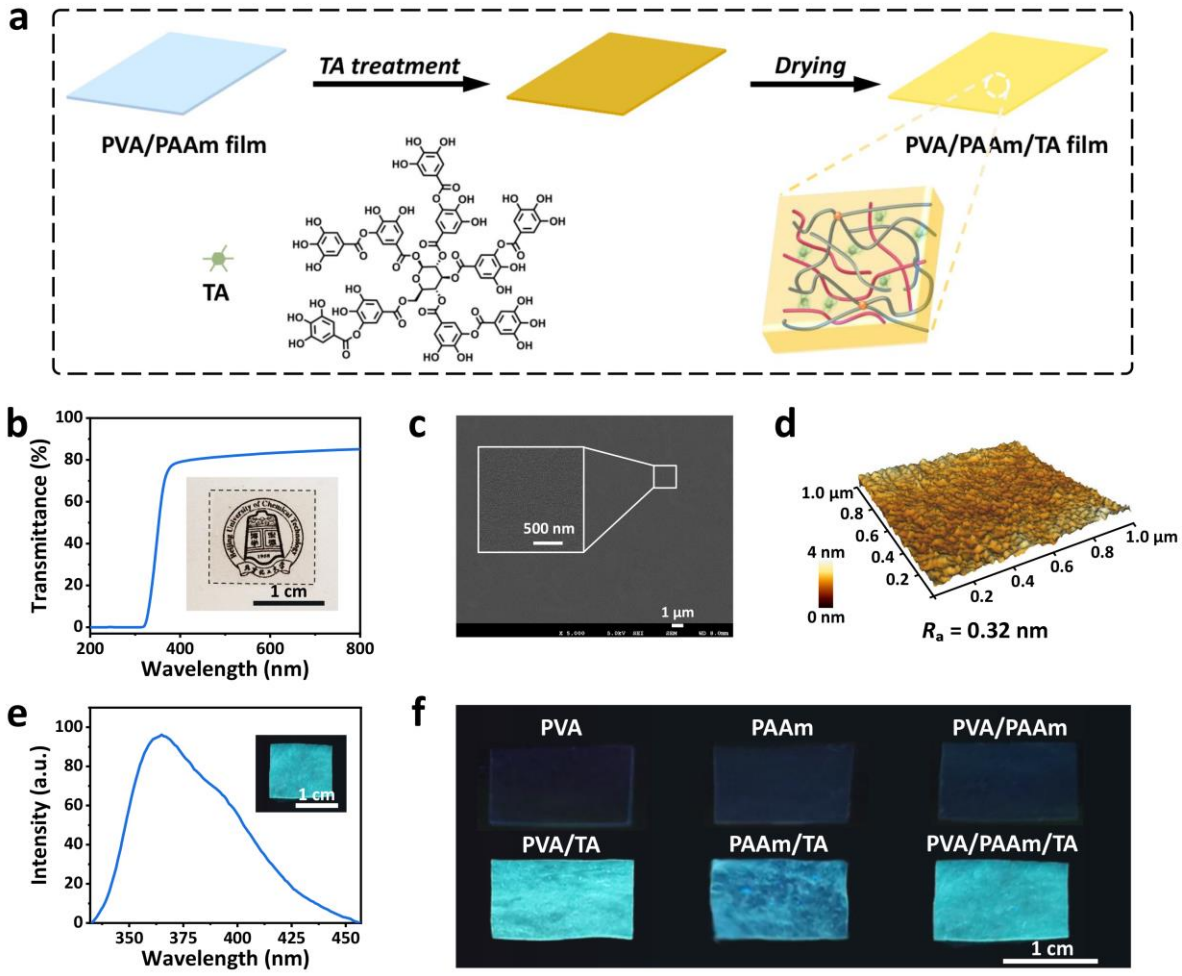

Figure 3. a) Schematic illustration of the fabrication of the PVA/PAAm/TA film. b) UV-vis spectrum of the PVA/PAAm/TA film. Inset shows the optical photo of the PVA/PAAm/TA film. c) Surface SEM image of the PVA/PAAm/TA film. Inset shows the local magnification. d) Surface AFM image of the PVA/PAAm/TA film. e) Fluorescence spectrum of the PVA/PAAm/TA film (excitation at 288 nm). Inset shows the photo of the PVA/PAAm/TA film

under UV light at 365 nm. f) Photos of the PVA, PAAm, PVA/PAAm, PVA/TA, PAAm/TA, and PVA/PAAm/TA films under UV light at 365 nm.

To verify the role of hydrogen bonding in the physical anchoring effect in depth, the peak fitting method was employed in ATR-FTIR region from 2980 to 3600 cm^{-1} that belonged to the stretching vibration of hydroxyl groups (υ_{O-H}) and amide groups (υ_{N-H}), and the corresponding peak assignments were summarized in Table S1. The vibration bands at 3218 cm^{-1} corresponded to the υ_{O-H} of PVA (Figure S9a, Supporting Information), and the υ_{N-H} of PAAm was represented by the vibration bands at 3324 and 3150 cm^{-1} (Figure S9b, Supporting Information). Regarding TA, the υ_{O-H} belonging to the phenolic hydroxyl groups was assigned at 3352 cm^{-1} due to existence of the aromatic structure (**Figure 4**a). As for the PVA/PAAm, the υ_{O-H} from PVA located at 3176 cm^{-1} and υ_{N-H} from PAAm appeared at 3291 and 3087 cm^{-1} (Figure S9c, Supporting Information). Compared with neat PVA and PAAm, this shift of wavenumbers revealed the hydrogen bonds between PVA and PAAm, consistent with the theoretical calculation results of hydrogen bonding between PVA and PAAm in Figure 1f. In addition, the peak fitting results of PVA/PAAm/TA revealed that the υ_{O-H} from PVA and TA were at 3147 and 3332 cm^{-1}, respectively, while the υ_{N-H} from PAAm located at 3234 and 3058 cm^{-1} (Figure 4b). All these peaks continued to shift to lower wavenumbers in comparison with TA and PVA/PAAm, clearly demonstrating the formation of hydrogen bond interactions of TA with PVA and PAAm. Meanwhile, the geometric structures of PVA-TA and PAAm-TA were optimized at the B3LYP-D3(BJ)/def2-SVP level based on DFT models, and their hydrogen bonding and intermolecular interaction energies were analyzed. As illustrated in Figure 4c, the bond strength was calculated to be -7.98 and -7.10 Kcal/mol for PVA-TA and PAAm-TA, respectively. And the intermolecular interaction energy between PVA and TA was -9.22 Kcal/mol, while -11.48 Kcal/mol between PAAm and TA (Figure 4d). These simulation results further confirmed that PVA and PAAm can anchor TA molecules via multiple hydrogen bonding interactions to endow the film with fluorescence.

These multiple hydrogen bonds can create a substantial amount of cross-linked networks, considerably enhancing the mechanical properties of PVA/PAAm/TA film. As shown in Figure 4e and f, the PVA/PAAm film had a tensile stress at break of 31.5 MPa and Young′s modulus of 2.3 GPa. Upon treatment of TA for 3 min, the stress at break and Young′s modulus increased to 61.7 MPa and 3.3 GPa, which demonstrated that the introduction of TA improved the mechanical performance of the film through the hydrogen bonding between polymers and TA. Further extending the treatment time of TA caused a progressive rise of the stress at break and

Young′s modulus, which reached the maximum value of 75.0 MPa and 7.1 GPa when 10 min was applied. Accordingly, 10 min was chosen as the optimized treatment time in the following research. In addition, to ensure that the processing had no influence on mechanical properties of the film, we established a blank group that was treated with only deionized water for 10 min. In comparison to the untreated film (0 min), the blank film maintained the Young's modulus of 2.2 GPa, proving that its mechanical property was not affected by the processing.

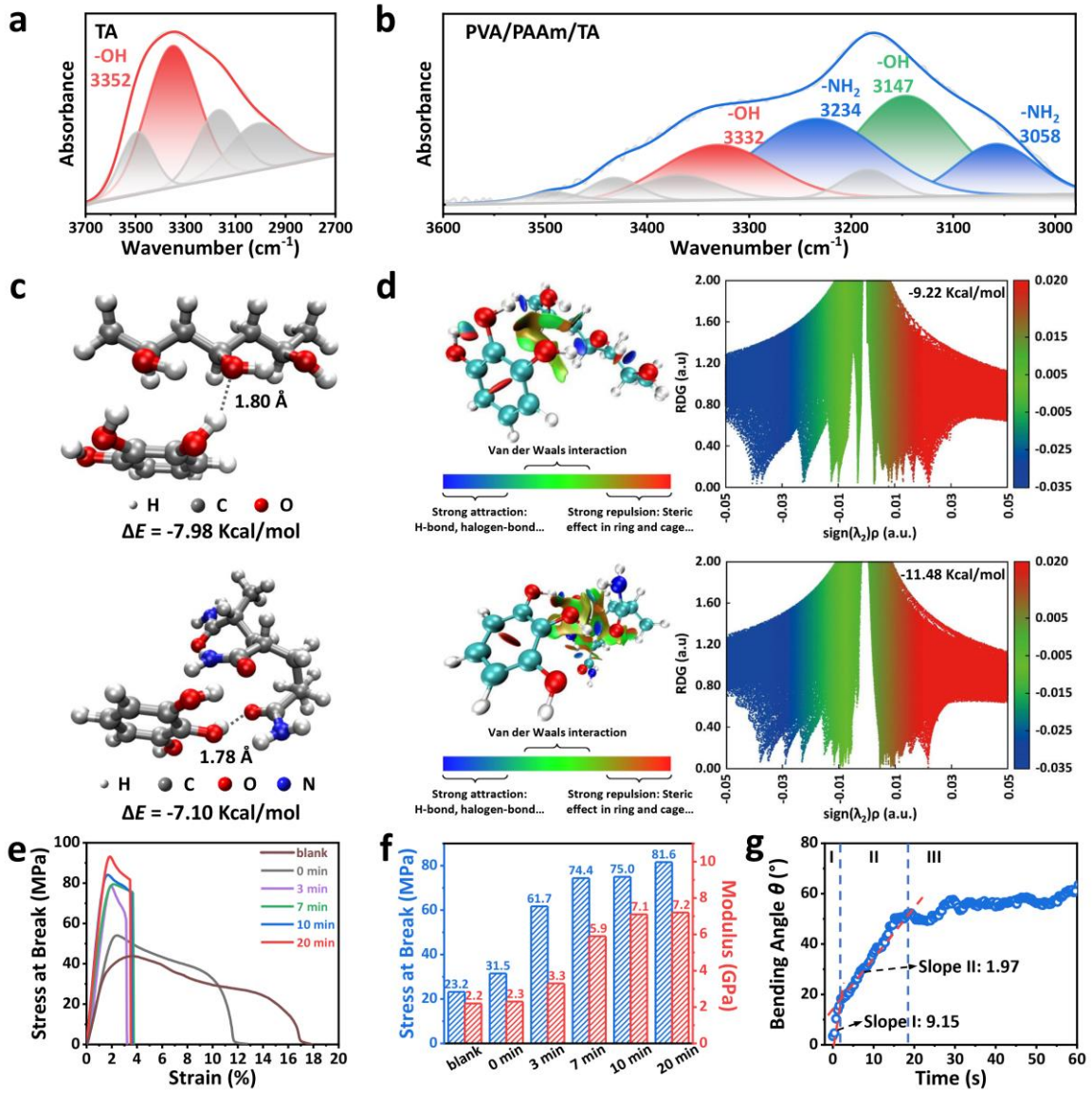

Figure 4. ATR-FTIR absorption peaks and their fitting curves of a) TA from 3700 to 2700 cm^{-1} and b) PVA/PAAm/TA from 3600 to 2980 cm^{-1}. c) Hydrogen bonding interactions of PVA-TA and PAAm-TA obtained by DFT. The distance of the hydrogen bond is indicated by the dotted line. d) Color-filled RDG (reduced density gradient) plots (isovalue = 0.5) and RDG vs sign(λ_2)ρ of PVA-TA and PAAm-TA obtained by DFT. e) Tensile strain-stress curves of the PVA/PAAm film upon treatment of deionized water (blank) and TA for different time. f)

Values of tensile stress at break and Young's modulus in e). g) Variation of bending angle of the PVA/PAAm/TA film upon exposure to the ΔRH of 55%.

Note that despite the improvement in fluorescence and mechanical properties, the introduction of TA had no significant effect on humidity actuation. The PVA/PAAm/TA film had a similar contact angle with the PVA/PAAm film (Figure S10, Supporting Information). The bending speed and holding time of the PVA/PAAm/TA film at ΔRH = 55% in stage I was slightly slowed down to 9.15° s^{-1} and 2 s (Figure 4g) because of the reduced swelling difference and the increased bending stress. Similarly, the bending speed in stage II was reduced to 1.97° s^{-1}. Even though, once the bending angle reached the maximum, the PVA/PAAm/TA film stayed stable and responded to humidity in less than 20 s, comparable with the PVA/PAAm film. In summary, the TA-induced physical crosslinking and intermolecular hydrogen bonding simultaneously endowed the PVA/PAAm/TA film with high optical transparency, good mechanical property, bright cyan emission, and fast humidity-response.

2.4 Humidity-driven in-situ viewable deformation of the patterned-PVA/PAAm/TA film

Figure 5a depicted the fabrication process of the patterned-PVA/PAAm/TA film. Initially, the TA-treated wet sponge segments were set down parallel on the PVA/PAAm film at a specific distance for 10 min. After removal of the sponge segments followed by drying, the patterned-PVA/PAAm/TA_{mn} film with parallel strip patterns were fabricated, where m was the width (mm) of TA-treated segments and n was the distance (mm) between TA-treated segments. By taking advantage of the patterned distribution of Young′s modulus between the TA-treated and untreated areas, the bending stress was restricted in an anisotropic manner when the patterned-PVA/PAAm/TA film was exposed to humidity source. As a result, its deformation can be well controlled in comparison with the random bending direction. More importantly, the local crosslinking area could be observed intuitively under UV light, which made it easier to in-situ recognize the programming mode of the actuator.

To optimize the geometric features on shape morphing, four patterned films of PVA/PAAm/TA_{24}, PVA/PAAm/TA_{22}, PVA/PAAm/TA_{21} and PVA/PAAm/TA_{31} were utilized to perform the humidity-driven deformation. The effect of m and n on driving performance was investigated by allowing the TA-treated segments to along in y-axis direction. As illustrated in Figure 5b, the PVA/PAAm/TA_{24}, PVA/PAAm/TA_{21}, and PVA/PAAm/TA_{22} produced bending along the y-axis in the humidity environment, as the bending stress required to be overcome during the bending was less along the y-axis direction. Conversely, the bending direction of the PVA/PAAm/TA_{31} was along the x-axis. This was because the disproportionate proportion of

the TA-treated areas made the bending stress along the y-axis was not significantly different from those along other directions. In addition, when the angle of the TA-treated strip with respect to the patterned films changed to 45° from 90°, similar deformation behaviors were observed. These results indicated that the deformation direction of the patterned films can be well controlled, and the programming models were directly observed under UV light. Here, the patterned-PVA/PAAm/TA_{22} was selected as an ideal film to quantitatively analyze the humidity-driven behavior under the ΔRH of 55%. As shown in Figure 5c, the bending speed of the patterned-PVA/PAAm/TA_{22} film at ΔRH = 55% in stage I was 9.58° s^{-1} and could hold 2 s, equivalent to that of PVA/PAAm/TA film. Afterwards, it attained the maximum bending angle of 80° at 22 s with a bending speed of 3.09° s^{-1} in stage II, while in stage III the bending angle was slightly increased. Moreover, the reversible bending-unbending can be repetitive over 15 times upon switching ΔRH of 55% and 0%, without apparent fatigue in continuous actuation cycles (Figure 5d, e).

Using the patterned-PVA/PAAm/TA_{22} film, a walking "crab" device and a smart lift were prepared by regulating the alignment of the parallel patterned structures. Figure 5f and Movie S2 (Supporting Information) showed the walking process of the "crab" actuator on an inclined rough substrate. When the humidity source was over the top surface of "crab" for 10 s, the "crab" bent into an arch. After the removal of the humidity source, the left claws of the "crab" that was subject to more friction functioned as the fixed point, while the right claws moved outward within 20 s as a result of the unbending. After repeating four cycles, the "crab" managed to move 1 cm in a single direction. In addition, the patterned-PVA/PAAm/TA_{22} film can be used as a smart mechanical lift. As shown in Figure 5g and Movie S3 (Supporting Information), when the ΔRH of 55% from the bottom to up was applied to the lift, it can elevate a weight of 168 mg (12 times the weight of the lift itself) in 4 s. Subsequently, the lift gradually held the weight to a height of 6.6 mm at 6 s and then hold it for 15 s, with a work in this lifting process calculated to be 11 μJ.

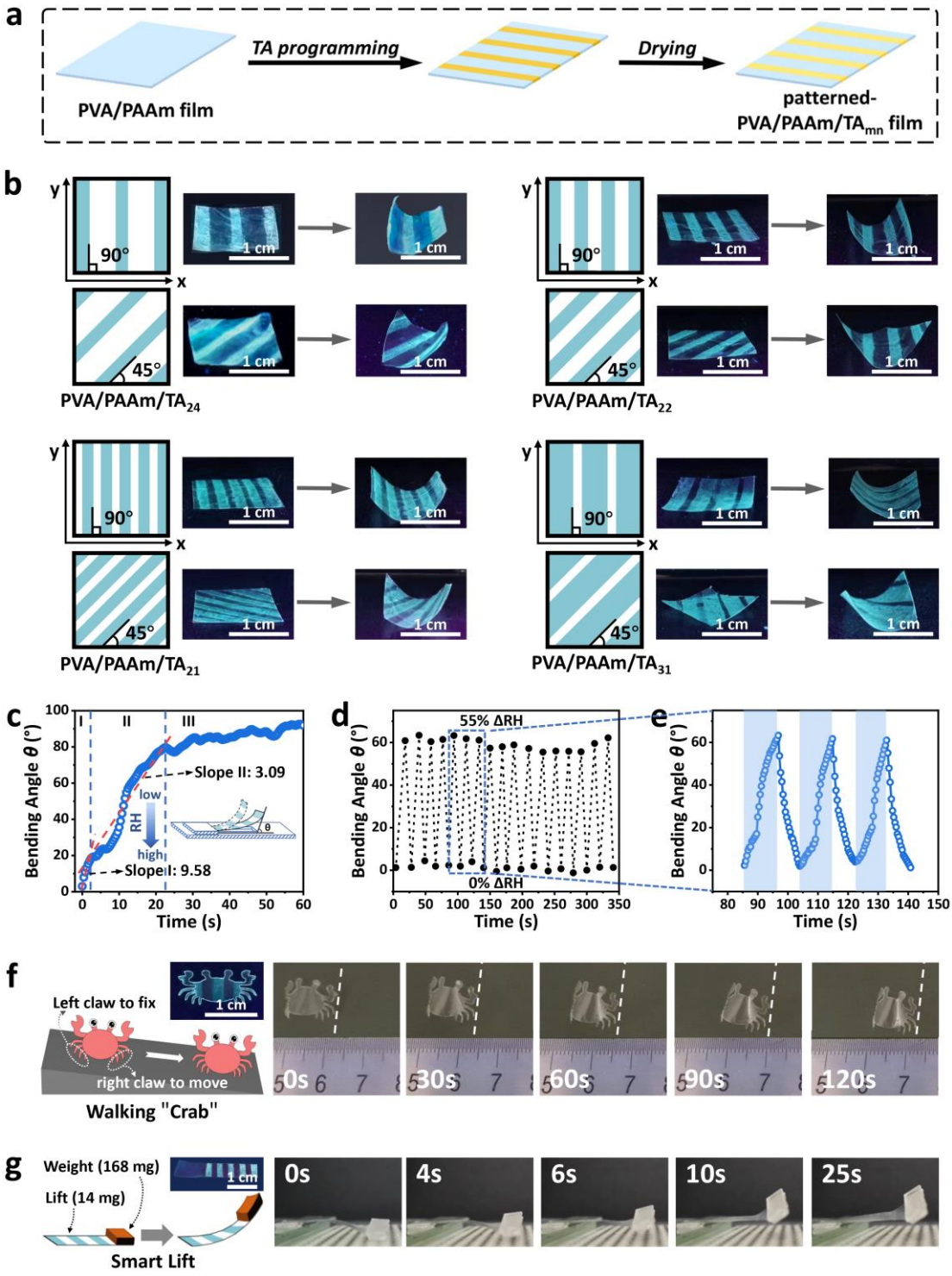

Figure 5. a) Schematic illustration of the fabrication of the patterned-PVA/PAAm/TA film. b) Schemes and photos of the humidity-driven deformation of the patterned-PVA/PAAm/TA$_{24}$, the patterned-PVA/PAAm/TA$_{22}$, the patterned-PVA/PAAm/TA$_{21}$, and the patterned-PVA/PAAm/TA$_{31}$ films under UV light at 365 nm with humidity source from the wet platform. c) Variation of bending angle of the patterned-PVA/PAAm/TA$_{22}$ film upon exposure to the ΔRH of 55%. Inset shows the schematic controlled deformation of the patterned-PVA/PAAm/TA$_{22}$ film with the decrease of RH from bottom to top. d) The reversible

motivation of the patterned-PVA/PAAm/TA_{22} film with continuously cycles of ΔRH = 55% and 0%. e) Three magnified cycles in d). Applications of the patterned-PVA/PAAm/TA_{22} film as f) a walking "crab" on an inclined rough substrate by periodically adding humidity for 10 s or removing humidity for 20 s, and g) a smart mechanical lift carrying a weight of 168 mg upon exposure to the ΔRH of 55%.

3. Conclusion

In conclusion, we have developed a viewable in-situ programmed humidity-driven monolayer actuator of PVA/PAAm/TA film, where PVA and PAAm were used as the hydrophilic substrate and natural TA was the patterning ink as a physical crosslinker. Benefiting from the multiple hydrogen bonding of TA with PVA and PAAm, the controllable modulus distribution of the monolayer film can be achieved precisely when patterning the polymer film using TA. More importantly, this anchoring effect on TA by physical crosslinking PVA and PAAm endowed TA molecules with bright fluorescence in solid state. The resulting PVA/PAAm/TA film simultaneously had high optical transparency (>80%), good mechanical property (tensile stress at break of 75.0 MPa, Young′s modulus of 7.1 GPa), cyan emission, and reversible fast humidity-response (0.04 s) under the ΔRH of 55%. After patterning, it can bend in different directions in a controlled manner in response to humidity gradient, and the programmed mode can be intuitively illuminated under UV light at 365 nm. Moreover, it showed promising applications in walking devices and smart mechanical lifts. This viewable and programmable approach will substantially aid the actual implementation of humidity-driven actuators in the fields of biomimicry, artificial muscles, and intelligent switches.

4. Experimental Section

Preparation of the PVA/PAAm film: Initially, PVA (1 g) was dissolved in 13.67 mL of deionized (DI) water at 95 ℃ with stirring, and then cooled to room temperature. After addition of AAm (2.01 g, 28.28 mmol), MBA (2.6 mg, 0.02 mmol) and APS (20.3 mg, 0.09 mmol), the solution was defoamed by centrifuging for 5 min (10000 rpm) and ultrasound for 30 min. Subsequently, the solution was transferred into a glass mold (6 cm × 6 cm × 1 mm) and polymerized in an oven at 60 ℃ for 90 min to afford a PVA/PAAm hydrogel. Lastly, by using a home-made biaxial pre-stretching device (Figure S11), the PVA/PAAm hydrogel was biaxial pre-stretched to a fixed ratio (3, 2, 2.5) and dried in an oven at 40 ℃ for 120 min, resulting in PVA/$PAAm_3$, PVA/$PAAm_{2.5}$, and PVA/$PAAm_2$ with the thickness of 15, 25, and 42 μm, respectively. The control film of polyethylene glycol/poly(N-isopropylacrylamide) (PEG/PNIPAm) was

prepared using the similar procedure of PVA/PAAm$_{2.5}$ film by replacing PVA and AAm with PEG and N-isopropylacrylamide, respectively.

Preparation of the fluorescent PVA/PAAm/TA film: A PVA sponge (5 cm × 5 cm × 2 mm) was immersed in the TA aqueous solution (0.24 mmol/mL) for 30 min, and then the TA-treated sponge was paved onto the PVA/PAAm film for 10 min. After removing the sponge, the treated film was left to dry at room temperature for 120 min. By rinsing the treated film with ethanol for 5 s, the fluorescent PVA/PAAm/TA film was finally obtained.

Preparation of the fluorescent patterned-PVA/PAAm/TA film: The PVA sponge (5 cm × 2 mm × 2/3 mm) was initially immersed in the TA aqueous solution (0.24 mmol/mL) for 30 min. After that, the TA-treated sponge segments were set down parallel on the PVA/PAAm film at a specific distance for 10 min. The processes that followed were same as those for the preparation of the PVA/PAAm/TA film. The patterned-PVA/PAAm/TA$_{mn}$ film was created by controlling the width of TA-treated and untreated segments, where m (mm) was the width of TA-treated segments and n (mm) was the distance between TA-treated segments.

Testing of the humidity-driven behaviors: The experiments were performed in a home-made humidity chamber (Figure S12), where the humidity was monitored by a hygrometer (ZL-TH10TP). The humidity chamber was consisted of an upper chamber and a bottom chamber with a window of 3 cm × 3 cm in the middle. The upper chamber had a constant RH of 20% supported by anhydrous $CaCl_2$, and the RH of the bottom chamber was controlled at 75% by fixing the water temperature in the bottom chamber at 25°C. When the film actuator was placed on the window, a ΔRH of 55% was provided, which caused the film actuator to continuously bend until reaching the maximum bending angle. Once the window was covered with a poly(methyl methacrylate) (PMMA) plate containing anhydrous $CaCl_2$, the ΔRH changed to 0% from 55%. In this case, the film actuator would unbend to its initial state. By opening and closing the window repetitively, the reversible bending and unbending in the humidity chamber can be achieved for cycles. The actuation performance of the film actuator was recorded using a camera Canon EOS M6, and the bending angle can be obtained by analyzing the recorded videos using Tracker software.

Supporting Information

Supporting Information is available from the Wiley Online Library or from the author.

Acknowledgements

This work is supported by the Open Fund of Anhui Province Key Laboratory of Environment-friendly Polymer Materials, and National Key Laboratory of Science and Technology on Advanced Composite (KZ42191814).

Conflict of Interest

The authors declare no conflict of interest.

Data Availability Statement

Research data are not shared.

Received: ((will be filled in by the editorial staff))
Revised: ((will be filled in by the editorial staff))
Published online: ((will be filled in by the editorial staff))

References

[1] Y. Forterre, J. M. Skotheim, J. Dumais, L. Mahadevan, *Nature* **2005**, *433*, 421.

[2] Z. Zhang, Z. Chen, Y. Wang, J. Chi, Y. Wang, Y. Zhao, *Small Methods* **2019**, *3*, 1900519.

[3] S. Poppinga, C. Zollfrank, O. Prucker, J. Ruhe, A. Menges, T. Cheng, T. Speck, *Adv. Mater.* **2018**, *30*, 1703653.

[4] C. Dawson, J. F. Vincent, A.-M. Rocca, *Nature* **1997**, *390*, 668.

[5] R. M. Erb, J. S. Sander, R. Grisch, A. R. Studart, *Nat. Commun.* **2013**, *4*, 1712.

[6] H. Kim, S. K. Ahn, D. M. Mackie, J. Kwon, S. H. Kim, C. Choi, Y. H. Moon, H. B. Lee, S. H. Ko, *Mater. Today* **2020**, *41*, 243.

[7] Y. Park, X. Chen, *J. Mater. Chem. A* **2020**, *8*, 15227.

[8] J. Wang, Y. Liu, Z. Cheng, Z. Xie, L. Yin, W. Wang, Y. Song, H. Zhang, Y. Wang, Z. Fan, *Angew. Chem. Int. Ed.* **2020**, *59*, 14029.

[9] H. Kim, K. R. Pyun, M. T. Lee, H. B. Lee, S. H. Ko, *Adv. Funct. Mater.* **2022**, *32*, 2110535.

[10] K. K. Kim, J. Choi, S. H. Ko, *Adv. Healthc. Mater.* **2021**, *10*, 2002286.

[11] K. W. Kwan, S. Li, N. Y. Hau, W. Li, S. Feng, A. H. W. Ngan, *Sci. Robot.* **2018**, *3*, eaat4051.

[12] X. Chen, D. Goodnight, Z. Gao, A. H. Cavusoglu, N. Sabharwal, M. DeLay, A. Driks,

O. Sahin, *Nat. Commun.* **2015**, *6*, 7346.

[13] D. Han, Y. Zhang, H. Jiang, H. Xia, J. Feng, Q. Chen, H. Xu, H. Sun, *Adv. Mater.* **2015**, *27*, 332.

[14] B. Shin, J. Ha, M. Lee, K. Park, G. H. Park, T. H. Choi, K. J. Cho, H. Y. Kim, *Sci. Robot*. **2018**, *3*, eaar2629.

[15] M. Weng, P. Zhou, L. Chen, L. Zhang, W. Zhang, Z. Huang, C. Liu, S. Fan, *Adv. Funct. Mater.* **2016**, *26*, 7244.

[16] M. Amjadi, M. Sitti, *ACS Nano* **2016**, *10*, 10202.

[17] J. Li, M. Wang, Z. Cui, S. Liu, D. Feng, G. Mei, R. Zhang, B. An, D. Qian, X. Zhou, Z. Liu, *J. Mater. Chem. A* **2022**, *10*, 25337.

[18] H. Chathuranga, I. Marriam, S. Chen, Z. Zhang, J. MacLeod, Y. Liu, H. Yang, C. Yan, *ACS Appl. Mater. Interfaces* **2022**, *14*, 16772.

[19] L. Yang, J. Cui, L. Zhang, X. Xu, X. Chen, D. Sun, *Adv. Funct. Mater.* **2021**, *31*, 2101378.

[20] L. Hu, Y. Wan, Q. Zhang, M. J. Serpe, *Adv. Funct. Mater.* **2020**, *30*, 1903471.

[21] P. Fratzl, F. G. Barth, *Nature* **2009**, *462*, 442.

[22] S. Lee, M. Lee, J. Lee, *Sens. Actuators B Chem.* **2021**, *332*, 129520.

[23] X. Li, J. Liu, D. Li, S. Huang, K. Huang, X. Zhang, *Adv. Sci.* **2021**, *8*, 2101295.

[24] Q. Zhu, Y. Jin, W. Wang, G. Sun, D. Wang, *ACS Appl. Mater. Interfaces* **2019**, *11*, 1440.

[25] G. Manikandan, A. Murali, R. Kumar, D. K. Satapathy, *ACS Appl. Mater. Interfaces* **2021**, *13*, 8880.

[26] T. Yang, H. Yuan, S. Wang, X. Gao, H. Zhao, P. Niu, B. Liu, B. Li, H. Li, *J. Mater. Chem. A* **2020**, *8*, 19269.

[27] J. Mu, G. Wang, H. Yan, H. Li, X. Wang, E. Gao, C. Hou, A. T. C. Pham, L. Wu, Q. Zhang, Y. Li, Z. Xu, Y. Guo, E. Reichmanis, H. Wang, M. Zhu, *Nat. Commun.* **2018**, *9*, 590.

[28] Q. Yan, L. Mao, B. Feng, L. Zhang, Y. Wu, W. Huang, *ACS Appl. Mater. Interfaces* **2021**, *13*, 7608.

[29] Y. Ge, H. Wang, J. Xue, J. Jiang, Z. Liu, Z. Liu, G. Li, Y. Zhao, *ACS Appl. Mater. Interfaces* **2021**, *13*, 38773.

[30] P. Won, K. K. Kim, H. Kim, J. J. Park, I. Ha, J. Shin, J. Jung, H. Cho, J. Kwon, H. Lee, S. H. Ko, *Adv. Mater.* **2021**, *33*, 2002397.

[31] H. Kim, H. Lee, I. Ha, J. Jung, P. Won, H. Cho, J. Yeo, S. Hong, S. Han, J. Kwon, K. J. Cho, S. H. Ko, *Adv. Funct. Mater.* **2018**, *28*, 1801847.

[32] H. Lee, H. Kim, I. Ha, J. Jung, P. Won, H. Cho, J. Yeo, S. Hong, S. Han, J. Kwon, K. J. Cho, S. H. Ko, *Soft Robot.* **2019**, *6*, 760.

[33] H. Jafari, P. Ghaffari-Bohlouli, S. V. Niknezhad, A. Abedi, Z. Izadifar, R. Mohammadinejad, R. S. Varma, A. Shavandi, *J. Mater. Chem. B* **2022**, *10,* 5873.

[34] Y. Wang, S. A. Sukhishvili, *Macromol. Rapid Commun.* **2017**, *38*, 1700242.

[35] R. Ricciardi, F. Auriemma, C. De Rosa, F. Laupretre, *Macromolecules* **2004**, *37*, 1921.

[36] S. Mishra, R. Bajpai, R. Katare, A. K. Bajpai, *J. Mater. Sci. Mater. Med.* **2006**, *17*, 1305.

[37] H. Kanniyappan, P. Thangavel, S. Chakraborty, V. Arige, V. Muthuvijayan, *Int. J. Biol. Macromol.* **2020**, *143*, 30.

[38] Y. Chen, C. Jiao, Y. Zhao, J. Zhang, H. Wang, *ACS Omega* **2018**, *3*, 11788.

[39] A. Ghafelebashi, S. Khosravani, M. H. Kazemi, F. Rajabi, M. C. Amiri, *Colloids Surf. A Physicochem. Eng. Asp.* **2022**, *650*, 129580.

[40] Y. He, K. Kong, Z. Guo, W. Fang, Z. Ma, H. Pan, R. Tang, Z. Liu, *Adv. Funct. Mater.* **2021**, *31*, 2101291.

[41] F. Azadikhah, A. R. Karimi, *React. Funct. Polym.* **2022**, *173*, 105212.

[42] W. Tian, J. Zhang, J. Yu, J. Wu, H. Nawaz, J. Zhang, J. He, F. Wang, *Adv. Opt. Mater.* **2016**, *4*, 2044.

[43] L. Jiao, Y. Liu, X. Zhang, G. Hong, J. Zheng, J. Cui, X. Peng, F. Song, *ACS Cent. Sci.* **2020**, *6*, 747.

[44] H. Xu, F. Xie, Y. Lu, P. Wei, J. Cai, *ACS Appl. Bio Mater.* **2021**, *4*, 5461.